# Desilicated ZSM-5 zeolites for an optimized xenon adsorption at very low pressure

Arthur Millet, Célian Courtney, Alban Gossard, Gabriel Couchaux, Pascale Mascunan, Alain Tuel, David Farrusseng

▶ **To cite this version:**

Arthur Millet, Célian Courtney, Alban Gossard, Gabriel Couchaux, Pascale Mascunan, et al.. Desilicated ZSM-5 zeolites for an optimized xenon adsorption at very low pressure. Microporous and Mesoporous Materials, 2023, 360, pp.112686. 10.1016/j.micromeso.2023.112686 . cea-04195984

**HAL Id: cea-04195984**
**https://cea.hal.science/cea-04195984**

Submitted on 5 Sep 2023

**HAL** is a multi-disciplinary open access archive for the deposit and dissemination of scientific research documents, whether they are published or not. The documents may come from teaching and research institutions in France or abroad, or from public or private research centers.

L'archive ouverte pluridisciplinaire **HAL**, est destinée au dépôt et à la diffusion de documents scientifiques de niveau recherche, publiés ou non, émanant des établissements d'enseignement et de recherche français ou étrangers, des laboratoires publics ou privés.

# Desilicated ZSM-5 zeolites for an optimized xenon adsorption at very low pressure

Arthur Millet,[1] Célian Courtney,[2] Alban Gossard,[1] Gabriel Couchaux,[2] Alain Tuel,[3] and David Farrusseng[3]

[1] *CEA, DES, ISEC, DMRC, Univ. Montpellier, Marcoule, France*

[2] *CEA, DAM, DIF, F-91297 Arpajon Cedex, France*

[3] *Université de Lyon, Université Claude Bernard Lyon 1, CNRS, IRCELYON - UMR 5256, Villeurbanne, France*

## Abstract

Rare gas selective capture using silver-loaded ZSM-5 zeolites was found to be really effective to recover xenon over a brand range of pressures ($10^{-5}$ to 10,000 ppm). However, understanding the close relationship between a zeolite microstructure and its silver loading is important for an optimized xenon adsorption in the case of molten salts reactors waste gas management. ZSM-5 with more or less structural defects were modified by alkaline treatment, leading to the formation of silanols defects and mesopores. After silver loading by cationic exchange, the concentration of strong acid sites increases generally of 30% for low desilication times and then decreases of approximatively 40% for high desilication times. Silver speciation was studied using different techniques (XRD, UV-vis, TEM…) in order to better understand the Ag-Xe interaction, which is still unclear in the literature. Finally, different Ag@ZSM-5 were compared to evaluate the role of zeolites structural defects in the formation and stabilization of silver NPs.


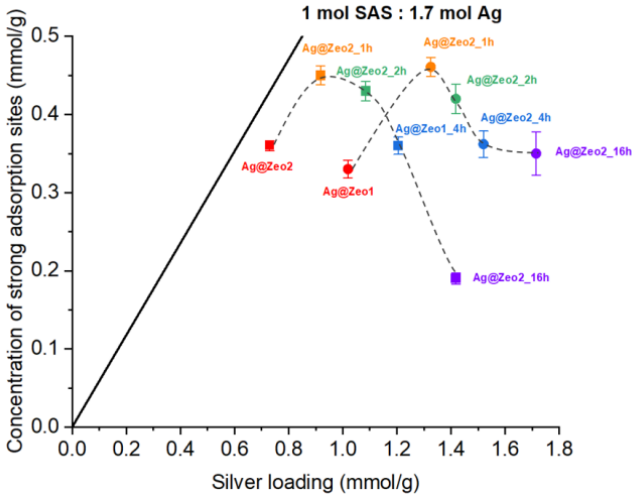

## 1. Introduction

Since 1940, much research has been conducted on molten salt reactors (MSRs), mainly in the USA, but also in Europe and China. MSRs are a Generation IV class of nuclear fission reactors that use a mixture of molten salts as their fuel and primary coolant [1–7]. The MSR concept is considered because it presents several advantages and some unique characteristics: it is potentially safer than actual light water reactors, but is also more efficient, sustainable and versatile [1,3,4]. During the operation of an MSR, many fission products are formed within the reactor core. Some of them are highly soluble in the molten salt mixture (such as lanthanides), but some noble gases (mainly xenon and krypton), mists and other chemicals that are not soluble in the salt will be evacuated with the cover gas [3]. Thus, radioactive isotopes of Xe and Kr are released as volatile fission products and have to be isolated using separation techniques such as cryogenic distillation or solid sorption [8–10]. The main goals are to manage radioactive wastes and atmospheric releases but also to reuse them in applications such as lighting [11], medicine [12,13] or chemical analysis [14].

Selective Xe adsorption on regenerable porous materials such as activated carbons, MOFs and zeolites has been found to be promising and economically attractive [3]. Since the 1970s, several research teams have shown that Xe can be strongly adsorbed on silver-loaded zeolites through the study of adsorption isotherms in the atmospheric pressure range [15–17], with the additional possibility of using silver-loaded zeolites for xenon and krypton for the reprocessing of spent nuclear fuel [18]. The beneficial effect of silver doping on Xe adsorption and Xe/Kr separation has been studied for numerous zeolites such as Ag-ZSM-5, Ag-mordenite and Ag-chabazite [18]. Recently, the Farrusseng research group (Daniel et al., Deliere et al., Monpezat et al.) has shown that Ag-exchanged ZSM-5 is the most effective material for atmospheric Xe capture and selective separation at very low pressure [19–24]. Grand-canonical Monte Carlo (GCMC) simulations can successfully characterize the adsorption of Xe on silver nanoparticles acting as strong adsorption sites at low concentration. A linear tendency was observed by Daniel et al., with a ratio of 2 moles of Ag for 1 mole of strong adsorption sites for BEA and ZSM-5 zeolites. It was also reported that Xe adsorption performance is better for zeolites with a low Si/Al ratio, because the quantity of exchangeable sodium cations and loaded silver increases, which leads to a higher concentration of strong adsorption sites [19].

Based on this observed tendency, we hypothesize that increasing the number of exchangeable sites by lowering the Si/Al ratio could be an approach to improve silver loading and selective xenon adsorption. However, it is impossible to obtain a ZSM-5 zeolite with a Si/Al ratio lower than approximately 10 with a direct synthesis [25,26]. This is why post-treatment desilication is used here to lower the Si/Al ratio. The aim of this study is to evaluate the impact of desilication of ZSM-5 zeolites on decreasing their Si/Al ratio and increasing the concentration of sodium-exchanged sites and, possibly, strong silver-based adsorption sites.

Two starting Na-ZSM-5 zeolites were studied to evaluate the impact of initial structural defects (mainly silanols and extra-framework Al) on the desilication process and potentially the formation/stabilization of the silver nanoparticles. One parent Na-ZSM-5 was synthesized using the typical tetrapropylammonium template, whereas the other parent Na-ZSM-5 is a commercial sample synthesized without an organic template.

## 2. Materials and methods

## 2.1. Materials

Two ZSM-5 zeolites were studied: a laboratory-synthesized ZSM-5 (Si/Al = 11.3, Na-form), hereafter named **Zeo1** and a commercial ZSM-5 from ACS Material (theoretical Si/Al = 12.5, H-form), hereafter named **Zeo2**. Sodium hydroxide NaOH (≥ 99.0%, pellets) was purchased from Supelco and silver nitrate $AgNO_3$ (ACS reagent, ≥ 99.0%) from Sigma-Aldrich. Aluminum sulfate hydrate $Al_2(SO_4).16H_2O$ (98%), tetrapropylammonium bromide TPABr (98%) and $SiO_2$ (Aerosil 200) were respectively supplied by Fluka, Sigma-Aldrich and Evonik.

## 2.2. Synthesis of Zeo1

Zeo1 (ZSM-5 zeolite, Si/Al=11.3) was synthesized using an organic template. For this, three solutions were prepared. For solution 1, 15.12 g (0.024 moles) of aluminum sulfate hydrate $Al_2(SO_4)_3.16H_2O$ were dissolved in 120 mL of deionized water. Then, solution 2 was prepared with 16 g of tetrapropylammonium bromide (TPABr, $6.10^{-2}$ moles) dissolved in 100 mL of deionized water. For solution 3.14 g of NaOH and 36 g of $SiO_2$ (Aerosil 200) were added to 180 mL of deionized water, with the $SiO_2$ being added slowly to the alkaline solution under very high stirring (paddle stirrer, 500-1000 rpm). Then, solution 1 was added to solution 3 under stirring, and finally solution 2 was added to the mixture. The complete solution was kept under high stirring for 30 minutes until a viscous gel was obtained. Then, 10 mL of a 1 N $H_2SO_4$ solution were added dropwise, and the resulting solution was stirred for 30 minutes. The thick gel was finally transferred to Teflon® containers and placed in stainless-steel autoclaves for 36 h at 170°C followed by 36 h at 190°C. The zeolite was recovered by filtration, washed three times with distilled water, dried at 80°C and calcined at 550°C under air for 12 h (1°C/min).

## 2.3. Alkaline treatment applied to zeolites

A mass of 2 g of zeolite was vigorously stirred in 100 mL of 0.2 M NaOH solution at 80°C for 1 h, 2 h, 4 h and 16 h respectively. The solution was then cooled down to room temperature. The zeolite suspension was filtered (with a 0.2 µm pore size filter), washed three times with deionized water and oven-dried at 80°C for 24 h. The different materials are referred to Zeo1_x or Zeo2_x with x representing the desilication time.

## 2.4.Silver loading

Silver loading was performed by a classic ion exchange procedure from the parent and desilicated zeolites. First, the determined mass of silver nitrate $AgNO_3$ was dissolved in deionized water (large excess of Ag, $n_{Ag}/n_{Al} \approx 3$). Then, 1 g of ZSM-5 zeolite was added to the $AgNO_3$ solution under vigorous stirring at 80°C for 5 h. The container was covered with aluminum foil to protect the silver nitrate from light degradation. The zeolite suspension was filtered (with a 0.2 µm pore size filter), washed three times with deionized water and oven-dried at 80°C for 24 h. Finally, the zeolite was treated at 673 K under $N_2$ gas flow for 4 h (15°C/min heating rate). This thermal treatment allows a stabilization of the materials prior to their use in the temperature-swing adsorption process for xenon adsorption, for which the desorption temperature is typically in the range of 523-623 K [21].

## 2.5. Characterization

The $N_2$ adsorption and desorption isotherms were performed at 77 K in a Micromeritics 3Flex version 5.02 apparatus. Prior to the adsorption analysis, the samples were treated under vacuum at 523 K for 3 hours with the Vac Prep and then for 1.5 hours at 523 K with the 3Flex. The

Brunauer–Emmett–Teller (BET) method was used to determine the total surface area, while the micropore and mesopore size characterization was carried out by NL-DFT. The Si/Al and Na/Al ratios in the zeolites were determined by X-ray fluorescence in a Panalytical Epsilon 4 apparatus. Ag concentration in the ZSM-5 after loading was evaluated using ICP-AES in a Thermo Scientific iCAP 6000 Series spectrometer. Prior to analysis, the samples were totally dissolved in an $HNO_3$/HF mixture and diluted in 2% $HNO_3$ (1/500). The diffuse reflectance FT-IR (DRIFTS) assembly from Spectra-Tech was used and placed in a Thermo 6700 spectrometer fitted with an MCT detector. DRIFTS spectra were recorded at 250°C under He. The DRIFTS background (128 scans) had been recorded over KBr under the same conditions. Typically, 32 scans at a resolution of 4 $cm^{-1}$ were performed to obtain a satisfactory signal-to-noise ratio. Prior to analysis, H-Zeo2 was sodium-exchanged with a 1.0 $mol.L^{-1}$ NaCl solution for 24 h at room temperature, with a final Na/Al molar ratio equal to 0.62. DRS UV-visible spectra were collected on a Shimadzu UV-2600 spectrophotometer equipped with an ISR-2600 integrating sphere from the same supplier. Spectra were performed at ambient pressure and temperature between 200 and 1000 nm. A $BaSO_4$ standard was used as a reference. All nuclear magnetic resonance (NMR) spectra were recorded on a Bruker Avance III 500 WB spectrometer equipped with a 4-mm double-bearing probe head. Samples were spun at 10 kHz in 4-mm zirconia rotors, and data were collected at room temperature. $^{29}Si$ and $^{27}Al$ magic-angle spinning (MAS) spectra were obtained using a "one-pulse" sequence. Pulse lengths and recycle delays were 4 µs ($\pi/3$) – 100s, and 1µs ($\pi/6$) – 1s for $^{29}Si$ and $^{27}Al$, respectively. X-ray powder diffraction (XRD) spectra were acquired using an X-Pert Pro PanAlytical diffractometer operating at 45 kW and 20 mA with the Cu-Kα radiation. The spectra were recorded between $2\theta = 5°$ and 70° for 42 min. Transmission electron microscopy analysis was performed using an ETEM FEI Titan (300-80 KeV) electron microscope on high vacuum mode. The samples were embedded in a polymer resin and cut using a Leica ultramicrotome; slices with targeted thicknesses of 50 nm were deposited on a TEM grid. The imaging was performed in bright-field mode (BF) and in high-angle annular dark-field monde (HAADF). Xe adsorption isotherms were performed at 298 K on a Belsorp MAX I (Microtrac-Bel) volumetric gas adsorption instrument with 5.0 grade Xe (Air Products). Prior to analysis, 250 mg of the solid samples were treated under a vacuum of $5.10^{-5}$ Pa at 573 K for at least 12 h. At $P/Po < 10^{-5}$ kPa, the adsorption equilibrium was considered to be reached when the pressure variation over 500 seconds was less than 0.3%. The xenon uptake was then measured at pressures varying from $10^{-5}$ kPa to 100 kPa.

## 3. Results

A summary of characterization results in the form of tabulated data is provided in Table 1. The alkaline treatment induces the selective elimination of Si from the zeolite network, which consequently decreases the Si/Al ratio, as observed in the literature [27–31]. When the desilication time increases, the Si/Al ratio decreases even more. The evolution of the Si/Al ratio is more pronounced for the laboratory-synthesized Zeo1 compared to the commercial Zeo2.

Table 1: Characterization of desilicated and silver-exchanged zeolites

| Zeolite | Si/Al[a] | Na/Al[b] | $S_{BET}$($m^2$/g)[c] | $V_{total}$ ($cm^3$/g)[d] | $V_{micro}$ ($cm^3$/g)[e] | $V_{meso}$ ($cm^3$/g)[f] | Silanols[g] | Silver loading (mmol/g)[b] | Ag/Al[b] |
|---|---|---|---|---|---|---|---|---|---|
| Zeo1 | 11.3 | 0.74 | 372 | 0.17 | 0.13 | 0.04 | 0.06 | 1.02 | 0.85 |
| Zeo1_1h | 9.5 | 0.69 | 385 | 0.28 | 0.13 | 0.15 | 0.13 | 1.33 | 0.91 |
| Zeo1_2h | 8.5 | 0.75 | 381 | 0.36 | 0.13 | 0.23 | 0.13 | 1.42 | 0.94 |
| Zeo1_4h | 7.9 | 0.76 | 389 | 0.38 | 0.13 | 0.25 | 0.16 | 1.52 | 0.92 |
| Zeo1_16h | 6.7 | 0.76 | 384 | 0.39 | 0.13 | 0.26 | 0.17 | 1.72 | 0.95 |
| Zeo2 | 14.6 | 0 | 399 | 0.19 | 0.14 | 0.05 | 0.07 | 0.73 | 0.66 |
| Zeo2_1h | 14.4 | 0.72 | 367 | 0.20 | 0.13 | 0.07 | 0.09 | 0.92 | 0.92 |
| Zeo2_2h | 13.8 | 0.73 | 385 | 0.26 | 0.14 | 0.12 | 0.10 | 1.08 | 0.99 |
| Zeo2_4h | 11.7 | 0.74 | 398 | 0.31 | 0.14 | 0.17 | 0.23 | 1.21 | 0.97 |
| Zeo2_16h | 10.7 | 0.77 | 390 | 0.42 | 0.14 | 0.28 | 0.25 | 1.42 | 0.95 |

[a] X-ray fluorescence (on Ag@ZSM-5 materials)
[b] ICP-AES (on ZSM-5 and Ag@ZSM-5)
[c] BET method (on ZSM-5)
[d] $N_2$ isotherm, at $P/P_0 = 0.994$ (on ZSM-5)
[e] $N_2$ isotherm, at $P/P_0 = 0.01$ (on ZSM-5)
[f] $N_2$ isotherm, Vtotal – Vmicro (on ZSM-5)
[g] Normalized area of the silanol peak, from DRIFTS spectra (on ZSM-5)

### 3.1. Characterization of the desilicated zeolites

#### 3.1.1. $N_2$ adsorption isotherm (77K)

Figure 1 shows the $N_2$ adsorption and desorption isotherms obtained at 77 K for all non-treated and modified Zeo1 and Zeo2. The BET surface area is the same for all ZSM-5 materials, at around 390 $m^2.g^{-1}$ (Table 1), which is a typical value for ZSM-5 zeolites [32,33]. At low pressures, the micropore filling is the same for all Zeo1 materials, as shown in Figure 1, which means that the zeolite network is not modified by the desilication process. The $N_2$ isotherm also shows that the micropore volume is equal to 0.113-0.14 $cm^3.g^{-1}$ for all materials (Table 1). The NL-DFT analysis suggests that the zeolite pore size (around 0.6 nm) is not affected by the alkaline treatment.

The isotherm hysteresis is characteristic of the creation of mesopores during the alkaline treatment and the elimination of Si from the zeolite network [27,28,34–36], which is entirely in keeping with the estimation of mesopore volume (Table 1) for both Zeo1 and Zeo2, determined from the total volume and micropore volume. The NL-DFT also shows a large mesopore diameter distribution varying from 5 nm to 35 nm. The formation of mesoporosity is different for the two zeolites studied. For Zeo1, mesopore formation is relatively significant for low desilication times, as the mesopore volume increases from 0.05 $cm^3.g^{-1}$ to 0.24 $cm^3.g^{-1}$ in the first 2 h (Table 1). The mesopore volume then increases much more slightly, from 0.24 to 0.27 $cm^3.g^{-1}$ during the following 14 h. For Zeo2, mesopore formation is more gradual, as the corresponding volume increases from 0.07 $cm^3.g^{-1}$ for Zeo2 to 0.14 $cm^3.g^{-1}$ for Zeo2_2h and 0.31 $cm^3.g^{-1}$ for Zeo2_16h. Thus, the structural properties of the zeolites (Si/Al ratio, extra-framework Al, crystallinity, grain size) seem to have an influence on the quantity of dissolved Si and on mesopore formation.

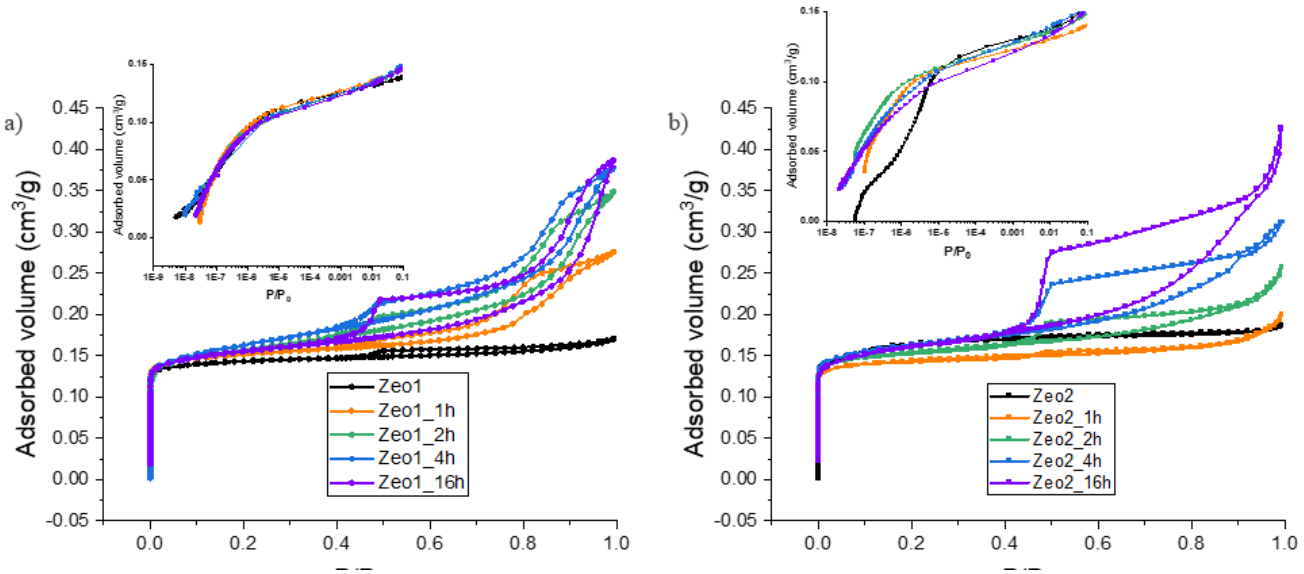


Figure 1: $N_2$ adsorption-desorption isotherms at 77 K for (a) non-treated and desilicated Zeo1, and (b) non-treated and desilicated Zeo2.

### 3.1.2. $^{27}$Al and $^{29}$Si MAS-NMR

$^{27}$Al MAS-NMR spectra were recorded on all non-modified and desilicated ZSM-5 and are presented in Figure 2. A peak at 56 ppm corresponding to tetra-coordinated Al from the zeolite network is visible for all Zeo1 and Zeo2 samples. Many research groups, such as Gil et al, Hoff et al. and others, have made the same observation for ZSM-5 zeolites [31,35,37]. The presence of hexa-coordinated Al at 0 ppm for Zeo2 suggests that a fraction of the aluminum is in an extra-framework position, certainly cause by some post synthesis treatments, and disappears after the alkaline treatment. Extra-framework Al were therefore solubilized by NaOH and washed away, as shown by several groups for ZSM-5 and ZSM-12 zeolites [35,38,39].

$^{29}$Si MAS-NMR spectra were only recorded on the non-modified and 16 h-desilicated Zeo1 and Zeo2 and are shown in Figure 2. For all materials, the -113 ppm signal is assigned to siloxane linkages (Si-O-Si), which is the most intense signal. The same peak corresponding to Si-O-Si

was observed by Gil et al. and Hoff et al., after desilication with an NaOH solution varying in concentration from 0.1 to 1.0 M [35,37]. The broad shoulder at -105 ppm corresponds to Si linked to one Al atom (Si-O-Al). This peak intensity increases after the alkaline treatment, because the Al/Si ratio is higher in the desilicated zeolite. The intensity of the signal at -95 ppm, corresponding to SiOH, also increases after treatment, which suggests the formation of silanol groups during the desilication process.

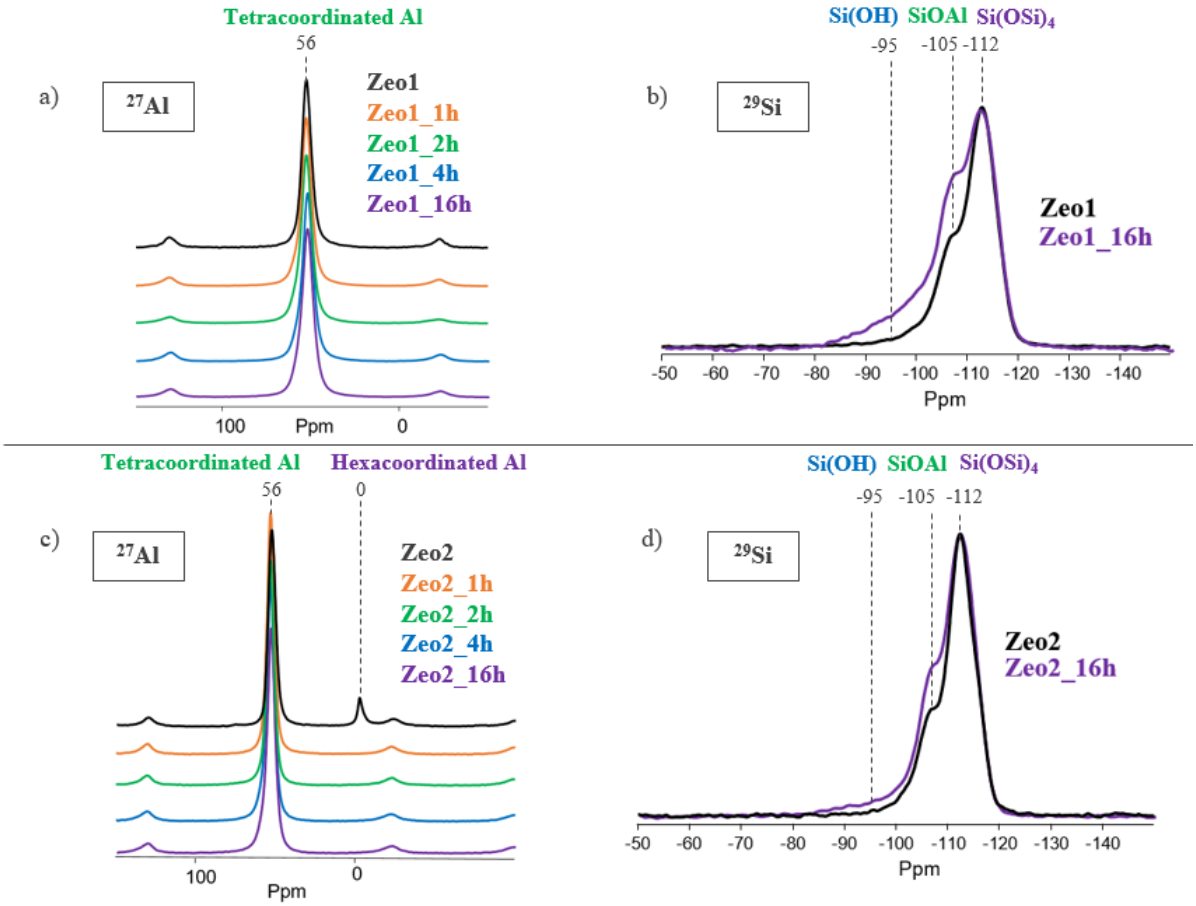


Figure 2: $^{27}$Al and $^{29}$Si MAS NMR for (a,b) non-treated and desilicated Zeo1, and for (c,d) non-treated and desilicated Zeo2.

### 3.1.3. DRIFTS

The signals from 3800 cm$^{-1}$ to 3300 cm$^{-1}$, corresponding to the OH-stretch vibration in the ZSM-5 zeolites, were corrected and normalized by the overtone area signal corresponding to the zeolite framework (1800 to 2100 cm$^{-1}$) [40]. Figure S1 (Supporting Information) presents the DRIFTS spectra for all Zeo1 and Zeo2.

For all Zeo1, the band at 3735 cm$^{-1}$ and the broad shoulder at 3720 cm$^{-1}$ are generally assigned in the literature to isolated silanol (Si-OH) groups, most of them being located on the external surface or in the mesopores, as found by Gabrienko et al. and Barbera et al. [41,42]. The normalized area of the band is reported in Table 1 for all non-modified and desilicated Zeo1. When the desilication time increases, the normalized area of the Si-OH band increases, meaning that silanol groups are formed during the alkaline treatment [35].

For non-modified Zeo2, the band at 3600 cm$^{-1}$ is attributed to isolated bridged Si-O(H)-Al groups [41–43]. Indeed, even if the H-Zeo2 was Na-exchanged prior to analysis, $H^+$ cations

remain present within the zeolite network. The band at 3671 $cm^{-1}$ is attributed to extra-framework Al-OH, which is in accordance with NMR studies for Zeo2. Both bands at 3600 and 3671 $cm^{-1}$ then disappear for all the desilicated Zeo2, because the alkaline treatment with NaOH removed the remaining $H^+$ cations and solubilized the extra-framework Al that was initially present, and then washed them away. Concerning the Si-OH, the observations are similar to those made for Zeo1, and the normalized area increases from 0.07 for Zeo2 to 0.25 for Zeo2_16h, as reported in Table 1.

These DRIFTS analyses performed on non-modified and desilicated zeolites finally serve to highlight the $H^+ \leftrightarrow Na^+$ exchange in NaOH solution, with an Na/Al molar ratio increase (Table 1), the elimination of extra-framework Al-OH species and the formation of silanol (Si-OH) groups.

## 3.2. Characterization of silver-loaded zeolites

### 3.2.1. Silver loading

All of the non-modified and desilicated Na-Zeo1 and Na-Zeo2 were silver-exchanged. Silver loading was determined by ICP-AES (Table 1), with the evolution of the Si/Al ratio during the desilication process illustrated in Figure 3.

For the silver-loaded parent zeolites Ag@Zeo1 and Ag@Zeo2 (desilication time = 0), the silver loadings are respectively equal to 11.0% wt and 7.9% wt, which is close to the values reported in the literature for similar materials [44–46].

Concerning Ag@Zeo1 materials, silver loading increases drastically at low desilication times, from 11.0% wt to 16.9% wt for Ag@Zeo1_2h, and then much more slightly at high desilication times (18.5% wt for Ag@Zeo1_16h). It is clear that when the Si/Al ratio decreases, the silver loading increases, thereby following the same trend. Moreover, it is also possible to compare the silver loading to the total pore volume and the quantity of silanols; they too follow a comparable evolution, as they all increase from low desilication time, as shown in Figure S2 (Supporting Information).

The silver loading for Ag@Zeo2 increases gradually from 7.9% wt to 14.5% wt for Ag@Zeo2_2h and then to 16.9% wt for Ag@Zeo2_16h. In this case, the Si/Al ratio for Zeo2 is globally higher than that of Zeo1, which leads to a lower silver loading. For all of the desilicated ZSM-5, the Si/Al ratio seems unsurprisingly to be the main factor directing the maximum silver loading. As expected, the duration of desilication affects the total pore volume and the mesopore volume (Table 1 and Figure S2).

In both cases, the alkaline treatment, even at low desilication time, leads to a large increase in the silver loading in the zeolite materials, due to a decrease in the Si/Al ratio and improved accessibility due to mesopore formation and the elimination of extra-framework Al.

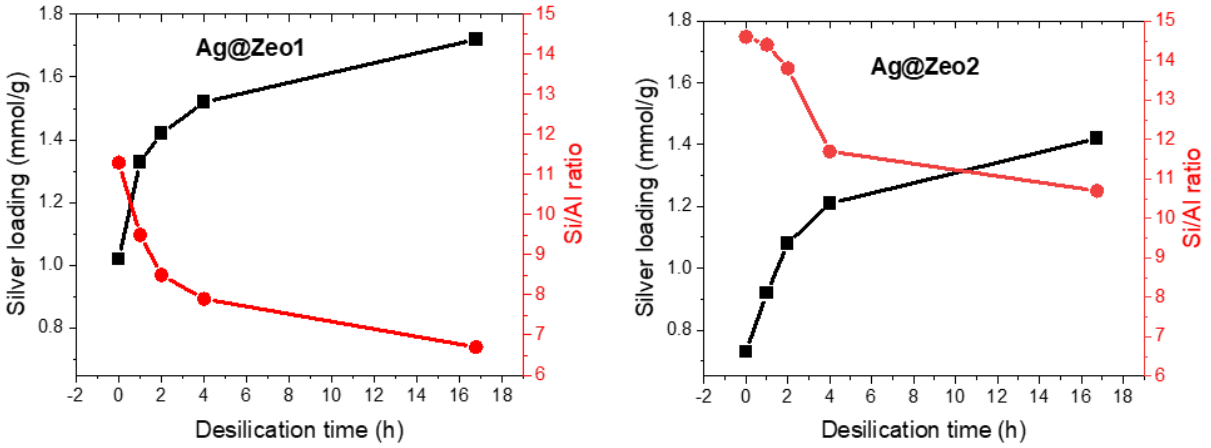


Figure 3: Evolution of silver loading (squares) and Si/Al ratio (dots) with the treatment time for non-treated and desilicated Zeo1 (on the left), and non-treated and desilicated Zeo2 (on the right).

### 3.2.2. X-ray diffraction

Figure S3 (Supporting Information) shows the X-ray diffraction patterns for the reference ZSM-5 and silver-loaded zeolites after heat treatment. For all materials, the five main peaks for ZSM-5 at $2\theta$ = 7.9°, 8.8°, 23.1°, 23.2° and 23.9° are detected, even after the alkaline treatment and silver doping [44,46].

No silver diffraction peak (for either metallic silver or silver oxide) is visible for Ag@Zeo1 materials. This can mean that the Ag nanoparticles, if any, are too small. On the other hand, the diffraction peaks of Ag(111) at 38.1° and Ag(200) at 44.4° indicate the formation of metallic silver nanoparticles in all Zeo2 after thermal treatment [46,47].

### 3.2.3. UV-visible spectroscopy

Figure 4 shows the UV-visible spectra for Ag/ZSM-5 before heat treatment (in black) and all heat-treated Ag@ZSM-5. For silver-exchanged Zeo1 and Zeo2 before heat treatment, a band at 212 nm representing isolated $Ag^+$ cations ($4d^{10} \rightarrow 4d^9 5s1$ electronic transition) and bands at 270 and 290 nm representing $Ag^+$ clusters are observed [48,49]. At this step, silver remains mainly under its cationic form in the zeolite structure.

The isolated and clustered $Ag^+$ adsorption bands are still detected in all silver-loaded Zeo1 and Zeo2 after heat treatment. The large band at 380 nm, which is generally attributed to reduced silver nanoparticles, becomes more intense as the desilication and the silver loading increase, meaning that more Ag nanoparticles are formed [48,49]. After heat treatment at 400°C under nitrogen flow, auto reduction of $Ag^+$ into $Ag^0$ can occur with $O_2$ release [50]. As the silver loading and mesoporosity increase during desilication, the intensity of the $Ag^0$ nanoparticle peak increases for both Zeo1 and Zeo2, due to the possible diffusion of nanoparticles accompanied by the Ostwald ripening mechanism. The assignment of the two bands at 305 nm and 325 nm is not very clear in the literature and is discussed in the next section [47,49,51].

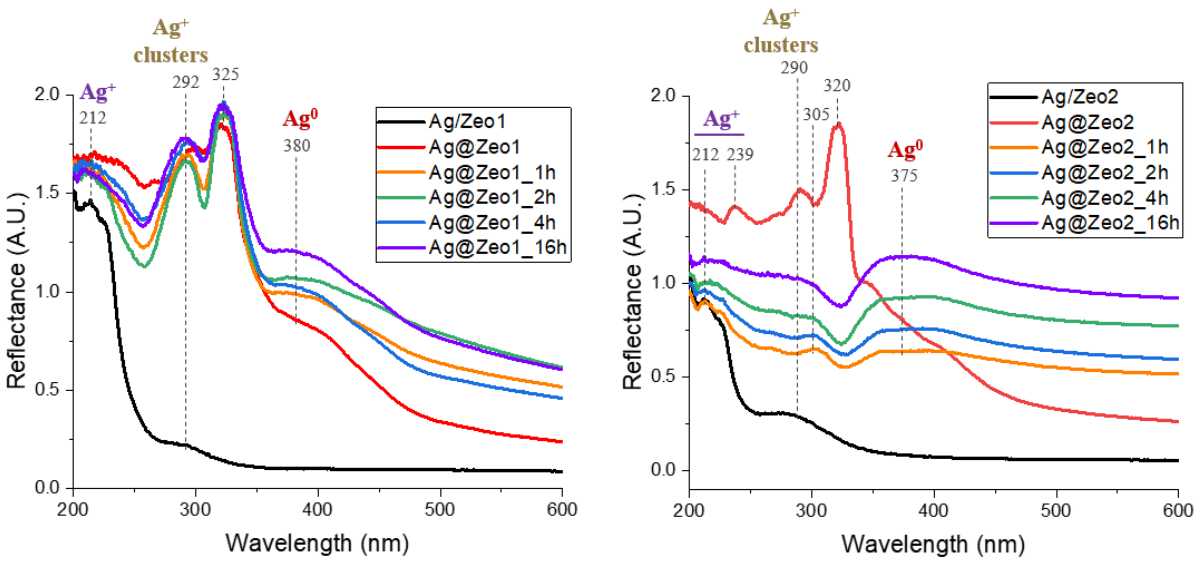


Figure 4: DRS UV-visible spectra of the silver-loaded non-treated and desilicated Zeo1 (on the left), and silver-loaded non-treated and desilicated Zeo2 (on the right).

### 3.2.4. Xenon adsorption isotherms

Xenon adsorption isotherms for all silver-loaded Zeo1 and Zeo2 are presented in Figure 5. For Zeo1 and Zeo2 before silver loading, no xenon is adsorbed for pressures lower than 0.3 kPa, as the zeolite adsorbs xenon only at high pressures. Indeed, xenon is not physically trapped in the zeolite network until a certain pressure is reached. After silver loading (red curves), the isotherms exhibit a different profile with two adsorption steps corresponding to two types of adsorption sites: a first step at low pressures from $10^{-5}$ to $10^{-1}$ kPa (concave-like) and a second step at pressures ranging from $10^{-1}$ to $10^{2}$ kPa (convex-like). Previous studies have associated the strong adsorption sites (first step) with silver nanoparticles and the weak adsorption sites (second step) with silver cationic species and the zeolite framework [19]. For desilicated Ag@ZSM-5, the Xe uptake seems to globally increase for the materials desilicated for 1 h or 2 h, while it decreases for longer desilication times. In order to quantitatively compare the adsorbents, it is possible to estimate some intrinsic parameters of the silver-doped zeolites by modeling the isotherms with a multi-nonlinear regression model (Sips model), as described in Equation 1, in which the first term describes the Xe adsorption on a weak adsorption site (zeolite) and the second term describes the adsorption on a strong adsorption site (silver).

Equation 1: Sips formula applied to Xe adsorption isotherms

$$q = q_1 + q_2 = N_1 \frac{(K_1 \cdot P)^{m_1}}{1 + (K_1 \cdot P)^{m_1}} + N_2 \frac{(K_2 \cdot P)^{m_2}}{1 + (K_2 \cdot P)^{m_2}}$$

where q is the adsorption capacity (mol.g$^{-1}$), N is the concentration of acid sites (mol.g$^{-1}$), K is the equilibrium constant (kPa$^{-1}$) and m is an exponent parameter (dimensionless, between 0 and 1) related to the heterogeneity of the site.

Different parameters can thus be extracted from this fitting. Notably, the $N_2$ parameter corresponds to the concentration of strong adsorption sites (Ag) and is an indicator of the Xe adsorption performance. This $N_2$ parameter is plotted as a function of silver loading for the different materials in Figure 6.

For both silver-loaded Zeo1 and Zeo2, the Xe adsorption performance increases for low desilication times. However, after 4 h or 16 h of desilication, the silver loading still increases, but the concentration of strong acid sites drastically decreases. These results will be discussed in more depth in the next section.

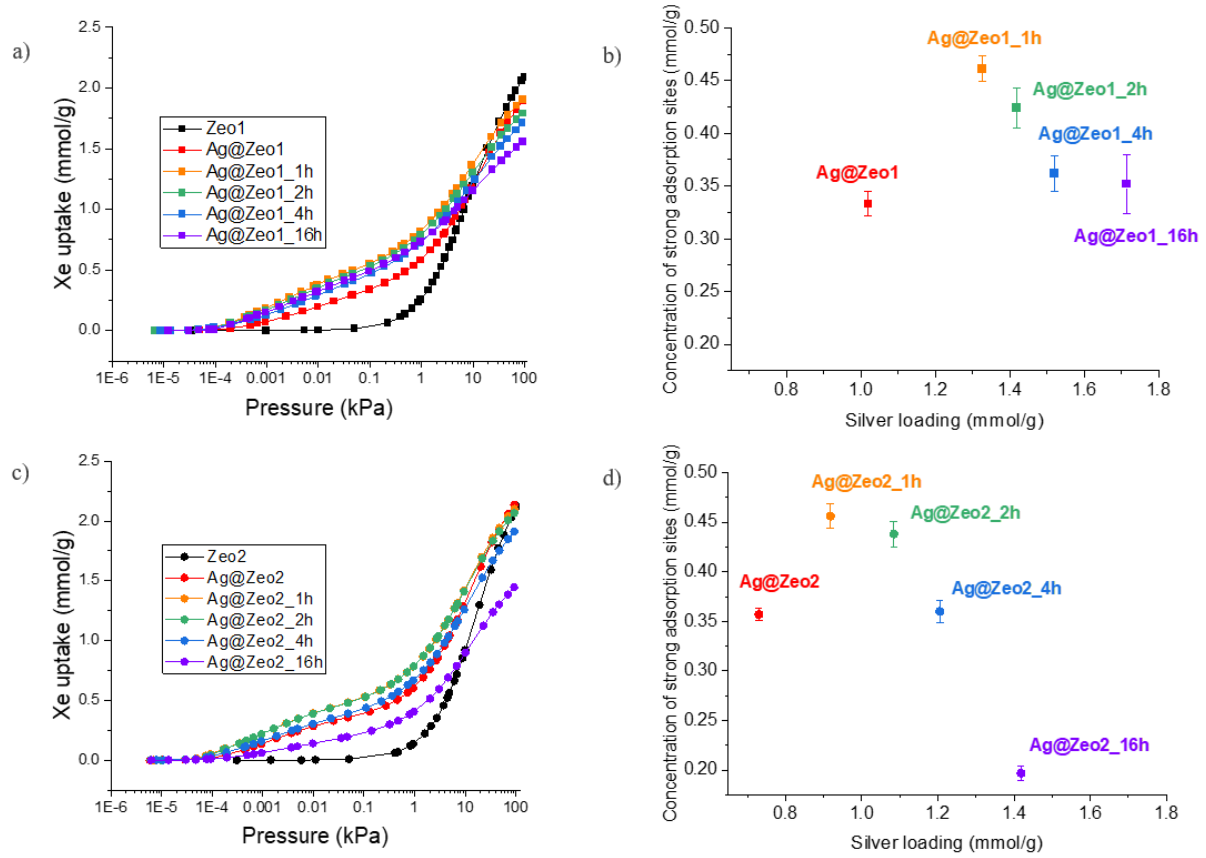


Figure 5: Xenon adsorption isotherms and corresponding evolution of the concentration of strong adsorption sites for (a,b) Zeo1 and Ag@Zeo1 non treated and desilicated, (c,d) Zeo2 and Ag@Zeo2 non treated and desilicated.

## 4. Discussion

Impact of low desilication

As expected, the Si/Al ratio decreases by desilication in alkaline medium. $Ag^+$ is inserted by cationic exchange and is thus correlated to the framework Al content (the exchange ratio being almost constant). After 1 h of desilication, the silver loading increases from 1.03 mmol.g$^{-1}$ for Ag@Zeo1 to 1.33 mmol.g$^{-1}$ for Ag@Zeo1_1h (30% increase), and from 0.73 mmol.g$^{-1}$ for Ag@Zeo2 to 0.92 mmol.g$^{-1}$ for Ag@Zeo2_1h (26% increase). This increase in silver loading leads to an increase in the concentration of strong adsorption sites of 40% for Ag@Zeo1_1h and 28% for Ag@Zeo2. This result is consistent with the hypothesis that the newly introduced silver is similar to the strong adsorption sites for Ag@ZSM-5 without desilication (in terms of oxidation state and cluster size). Indeed, no peak at 380 nm corresponding to Ag nanoparticles was detected using UV-visible spectroscopy for these materials, with the main peaks being located at 290 nm, 305 nm and 325 nm. The peak at 290 nm corresponds to $Ag^+$ clusters, while the two other peaks could be assigned to small $Ag_n^0$ clusters (a few atoms, $n < 7$), or at least

clusters of low charge [48,49,52]. These clusters are well dispersed in all Ag@ZSM-5 and Ag@ZSM-5_1h, which leads to a high specific surface area in contact with Xe and a higher concentration of strong adsorption sites.

Impact of severe desilication

After more than 2 h of desilication, the increase of the silver loading leads this time to a decrease of the concentration of strong adsorption sites for the two Ag-ZSM-5 zeolites. For Zeo1, there is a decrease of 10% from Ag@Zeo1_1h to Ag@Zeo1_2h, and of 32% from Ag@Zeo1_1h to Ag@Zeo1_16h. Concerning Zeo2, it leads to a 5% decrease from Ag@Zeo2-1h to Ag@Zeo2_2h, and 32% from Ag@Zeo2_1h to Ag@Zeo2_16h. This result can be explained by the lower concentration of strong adsorption sites. We can hypothesize a decrease in the dispersion of silver clusters. The high Ag concentration leads to the formation of silver clusters or particles whose core atoms cannot be adsorption sites that interact with Xe. These particles can be formed by Ostwald ripening during the thermal treatment at 400°C and stabilized in the mesoporous cavities formed by desilication". Nanoparticles are particularly visible by TEM for Ag@Zeo1_16h and Ag@Zeo2_16h, as shown in Figures S4 and S5. For both zeolites, the increase in the $Ag^0$ signal at 380 nm can be seen using UV-visible spectroscopy when the concentration of Ag increases, indicating the formation of larger Ag nanoparticles.

Comparison between Zeo1 and Zeo2

Differences are visible between Zeo1 and Zeo2 during desilication. $^{27}$Al NMR studies suggest that Zeo2 has a fraction of extra-framework Al that is dissolved under alkaline conditions. Indeed, this extra-framework Al is not a ionic exchange site, which leads to a relatively low Ag/Al molar ratio (0.66) for Zeo2, compared to approximately 0.95 for all other materials with no extra-framework Al, as shown in Table 1. This difference in structural defects between Zeo1 and Zeo2 can thus explain the lesser formation of mesoporosity and the Si/Al ratio decrease for Zeo2 as compared to a defect-free ZSM-5 such as Zeo1. But surprisingly, even though Zeo1 has a lower Si/Al ratio than Zeo2 and presents no defects (no extra-framework Al and no silanols), Ag@Zeo1 has a lower concentration of strong sites compared to Ag@Zeo2. Ag@Zeo1 is also far from the linear 1:1.7 trend found by Daniel et al [19], as shown in Figure 7, while commercial Ag@Zeo2 was found to be very close to it. We can hypothesize that ZSM-5 zeolites with structural defects facilitate the stabilization of strong adsorption sites, which could be more or less charged silver clusters.

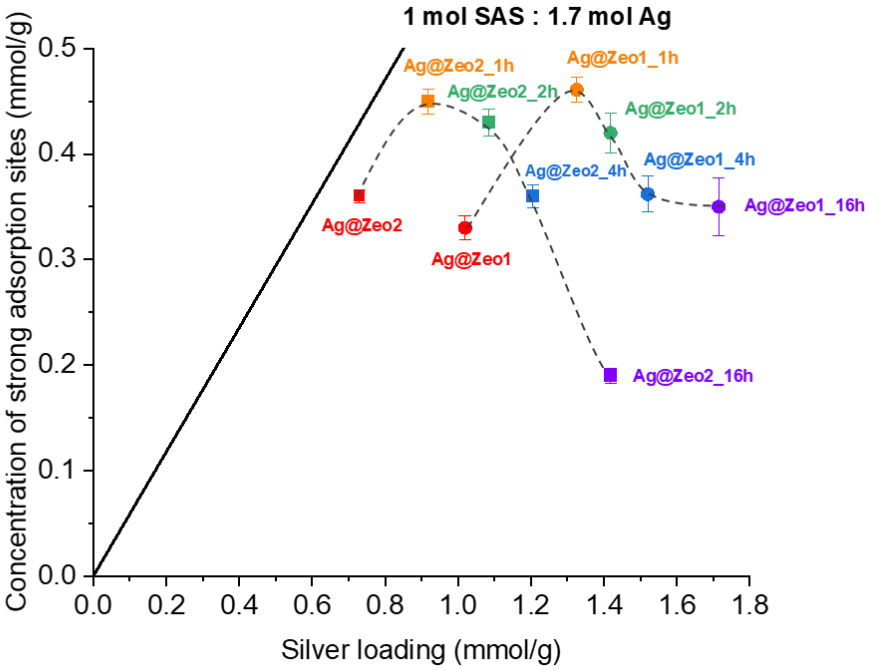


Figure 6: Evolution of the concentration of strong adsorption sites for all silver-loaded ZSM-5, compared to the linear 1:1.7 trend.

## 5. Conclusion

We have shown here that light desilication of this parent ZSM-5 makes it possible to significantly increase xenon uptake at very low pressure. The desilication creates a larger concentration of Al in the zeolite and thus enables a larger concentration of silver to be loaded. Yet we found that for severe desilication, decreased xenon uptake is observed, likely due to the facilitated formation of silver particles that are not useful for xenon uptake.

It appears that a concentration of 0.5 mmol/g of strong adsorption sites is a maximum achievable value for the Ag-ZSM-5 system.

Surprisingly, we found that the parent ZSM-5 zeolite prepared by organic templating yields Ag-ZSM-5 with a similar concentration of strong adsorption sites but at higher silver loading. We hypothesize that silanol defects present in the commercial zeolite may be responsible for the stabilization of silver clusters.

## Acknowledgments

This work was supported by ORANO.

The authors thank IRCELyon Scientific Services for sample characterization using TEM, DRIFTS, X-ray fluorescence and $N_2$ isotherms (Laurence Burel, Lucian Roiban, Frederic Meunier and Pascale Mascunan).

The authors are grateful to Pascal Antonucci for his help with X-ray diffraction characterization.

References:


1. J. Serp, M. Allibert, O. Beneš, S. Delpech, O. Feynberg, V. Ghetta, D. Heuer, D. Holcomb, V. Ignatiev, J.L. Kloosterman, L. Luzzi, E. Merle-Lucotte, J. Uhlíř, R. Yoshioka, D. Zhimin, *Progress in Nuclear Energy*, 77 (2014) 308–319.
2. J.C. Gehin, D.E. Holcomb, G.F. Flanagan, B.W. Patton, R.L. Howard, T.J. Harrison, Fast Spectrum Molten Salt Reactor Options, (2011).
3. J. Mcfarlane, B. Riley, D. Holcomb, A. Lines, H. Andrews, S. Bryan, S. Chapel, N.D. Ezell, H. Felmy, M. Greenwood, P. Humrickhouse, K. Myhre, Molten Salt Reactor Engineering Study for Off-Gas Management, (2020).
4. C. Degueldre, R. Dawson, I. Cooley, E. Besley, *Medicine in Novel Technology and Devices*, 10 (2021) 100057.
5. B.M. Elsheikh, *Journal of Radiation Research and Applied Sciences*, 6 (2013) 63–70.
6. D. LeBlanc, *Nuclear Engineering and Design*, 240 (2010) 1644–1656.
7. H.G. MacPherson, *Nuclear Science and Engineering*, 90 (1985) 374–380.
8. E. Aprile, J. Aalbers, F. et al Agostini, *Eur. Phys. J. C*, 77 (2017) 275.
9. R.E. Bazan, M. Bastos-Neto, A. Moeller, F. Dreisbach, R. Staudt, *Adsorption*, 17 (2011) 371–383.
10. L. Deliere, (n.d.) 240.
11. T. Shiga, Y. Ikeda, S. Mikoshiba, S. Shinada, *J. Light & Vis. Env.*, 25 (2001) 10–15.
12. P.V. Joshi, K.C. Jagadeesan, R.B. Manolkar, A.R. Mathakar, V. Chirayil, S.V. Thakare, A. Dash, M.R.A. Pillai, *Ind. Eng. Chem. Res.*, 51 (2012) 8575–8582.
13. L. Gallego Manzano, S. Bassetto, N. Beaupere, P. Briend, T. Carlier, M. Cherel, J.-P. Cussonneau, J. Donnard, M. Gorski, R. Hamanishi, F. Kraeber Bodéré, P. Le Ray, O. Lemaire, J. Masbou, S. Mihara, E. Morteau, L. Scotto Lavina, J.-S. Stutzmann, T. Tauchi, D. Thers, *Nuclear Instruments and Methods in Physics Research Section A: Accelerators, Spectrometers, Detectors and Associated Equipment*, 787 (2015) 89–93.
14. J. Fraissard, T. Ito, *Zeolites*, 8 (1988) 350–361.
15. *Proc. R. Soc. Lond. A*, 320 (1970) 289–308.
16. *Proc. R. Soc. Lond. A*, 326 (1972) 315–330.
17. *Proc. R. Soc. Lond. A*, 326 (1972) 331–345.
18. K. Munakata, S. Kanjo, S. Yamatsuki, A. Koga, D. Ianovski, *Journal of Nuclear Science and Technology*, 40 (2003) 695–697.
19. C. Daniel, A. Elbaraoui, S. Aguado, M.-A. Springuel-Huet, A. Nossov, J.-P. Fontaine, S. Topin, T. Taffary, L. Deliere, Y. Schuurman, D. Farrusseng, *J. Phys. Chem. C*, 117 (2013) 15122–15129.
20. L. Deliere, S. Topin, B. Coasne, J.-P. Fontaine, S. De Vito, C. Den Auwer, P.L. Solari, C. Daniel, Y. Schuurman, D. Farrusseng, *J. Phys. Chem. C*, 118 (2014) 25032–25040.
21. L. Deliere, B. Coasne, S. Topin, C. Gréau, C. Moulin, D. Farrusseng, *Chem. Eur. J.*, 22 (2016) 9660–9666.
22. A. Monpezat, G. Couchaux, V. Thomas, A. Artheix, L. Deliere, C. Gréau, S. Topin, B. Coasne, L. Roiban, L. Cardenas, D. Farrusseng, *Catalysts*, 9 (2019) 686.
23. A. Monpezat, S. Topin, L. Deliere, D. Farrusseng, B. Coasne, *Ind. Eng. Chem. Res.*, 58 (2019) 4560–4571.
24. A. Monpezat, S. Topin, V. Thomas, C. Pagis, M. Aouine, L. Burel, L. Cardenas, A. Tuel, A. Malchère, T. Epicier, D. Farrusseng, L. Roiban, *ACS Appl. Nano Mater.*, 2 (2019) 6452–6461.
25. M.M. Pereira, E.S. Gomes, A.V. Silva, A.B. Pinar, M.-G. Willinger, S. Shanmugam, C. Chizallet, G. Laugel, P. Losch, B. Louis, *Chem. Sci.*, 9 (2018) 6532–6539.
26. Y. Zhai, X. Zhang, F. Wang, G. Lv, T. Jiang, Y. Wu, M. Li, M. Li, Q. Zhang, Y. Liu, *ACS Appl. Mater. Interfaces*, 13 (2021) 15246–15260.
27. J.C. Groen, L.A.A. Peffer, J.A. Moulijn, J. Pérez-Ramírez, *Colloids and Surfaces A: Physicochemical and Engineering Aspects*, 241 (2004) 53–58.
28. J.C. Groen, J.A. Moulijn, J. Pérez-Ramírez, *Microporous and Mesoporous Materials*, 87 (2005) 153–161.

29. K. Sadowska, A. Wach, Z. Olejniczak, P. Kuśtrowski, J. Datka, *Microporous and Mesoporous Materials*, 167 (2013) 82–88.
30. K. Sadowska, K. Góra-Marek, M. Drozdek, P. Kuśtrowski, J. Datka, J. Martinez Triguero, F. Rey, *Microporous and Mesoporous Materials*, 168 (2013) 195–205.
31. K. Sadowska, K. Góra-Marek, J. Datka, *Vibrational Spectroscopy*, 63 (2012) 418–425.
32. L. Shirazi, E. Jamshid, M.R. Ghasem, *Cryst. Res. Technol.*, 43 (2008) 1300–1306.
33. L. Desmurs, A. Galarneau, C. Cammarano, V. Hulea, C. Vaulot, H. Nouali, B. Lebeau, T.J. Daou, C. Vieira Soares, G. Maurin, M. Haranczyk, I. Batonneau-Gener, A. Sachse, *ChemNanoMat*, 8 (2022).
34. J.C. Groen, W. Zhu, S. Brouwer, S.J. Huynink, F. Kapteijn, J.A. Moulijn, J. Pérez-Ramírez, *J. Am. Chem. Soc.*, 129 (2007) 355–360.
35. B. Gil, Ł. Mokrzycki, B. Sulikowski, Z. Olejniczak, S. Walas, *Catalysis Today*, 152 (2010) 24–32.
36. K. Mlekodaj, K. Tarach, J. Datka, K. Góra-Marek, W. Makowski, *Microporous and Mesoporous Materials*, 183 (2014) 54–61.
37. T.C. Hoff, D.W. Gardner, R. Thilakaratne, J. Proano-Aviles, R.C. Brown, J.-P. Tessonnier, *Applied Catalysis A: General*, 529 (2017) 68–78.
38. Ł. Mokrzycki, B. Sulikowski, Z. Olejniczak, *Catal Lett*, 127 (2009) 296–303.
39. M. Milina, S. Mitchell, Z.D. Trinidad, D. Verboekend, J. Pérez-Ramírez, *Catal. Sci. Technol.*, 2 (2012) 759.
40. M. Lions, C. Daniel, B. Coasne, F. Meunier, A. Tuel, D. Farrusseng, *J. Phys. Chem. C*, 125 (2021) 22890–22897.
41. A.A. Gabrienko, I.G. Danilova, S.S. Arzumanov, L.V. Pirutko, D. Freude, A.G. Stepanov, *J. Phys. Chem. C*, 122 (2018) 25386–25395.
42. K. Barbera, F. Bonino, S. Bordiga, T.V.W. Janssens, P. Beato, *Journal of Catalysis*, 280 (2011) 196–205.
43. H.D. Setiabudi, A.A. Jalil, S. Triwahyono, N.H.N. Kamarudin, R.R. Mukti, *Applied Catalysis A: General*, 417–418 (2012) 190–199.
44. M.S.-L. Yee, P.S. Khiew, Y.F. Tan, W.S. Chiu, Y.-Y. Kok, C.-O. Leong, *Microporous and Mesoporous Materials*, 218 (2015) 69–78.
45. E. Kolobova, A. Pestryakov, A. Shemeryankina, Y. Kotolevich, O. Martynyuk, H.J. Tiznado Vazquez, N. Bogdanchikova, *Fuel*, 138 (2014) 65–71.
46. C. Shi, M. Cheng, Z. Qu, X. Bao, *Journal of Molecular Catalysis A: Chemical*, 235 (2005) 35–43.
47. M. Chebbi, B. Azambre, L. Cantrel, A. Koch, *J. Phys. Chem. C*, 120 (2016) 18694–18706.
48. M. Chebbi, B. Azambre, L. Cantrel, M. Huvé, T. Albiol, *Microporous and Mesoporous Materials*, 244 (2017) 137–150.
49. R. Bartolomeu, R. Bértolo, S. Casale, A. Fernandes, C. Henriques, P. da Costa, F. Ribeiro, *Microporous and Mesoporous Materials*, 169 (2013) 137–147.
50. P.A. Jacobs, J.B. Uytterhoeven, H.K. Beyer, *J. Chem. Soc., Faraday Trans. 1*, 75 (1979) 56.
51. E. Kolobova, A. Pestryakov, G. Mamontov, Yu. Kotolevich, N. Bogdanchikova, M. Farias, A. Vosmerikov, L. Vosmerikova, V. Cortes Corberan, *Fuel*, 188 (2017) 121–131.
52. A.N. Pestryakov, A.A. Davydov, *Journal of Electron Spectroscopy and Related Phenomena*, 74 (1995) 195–199.